THE GEOLOGICAL SOCIETY OF AMERICA®

BULLETIN

ISSN 0016-7606 VOL. 124 NO. 5/6 MAY/JUNE 2012

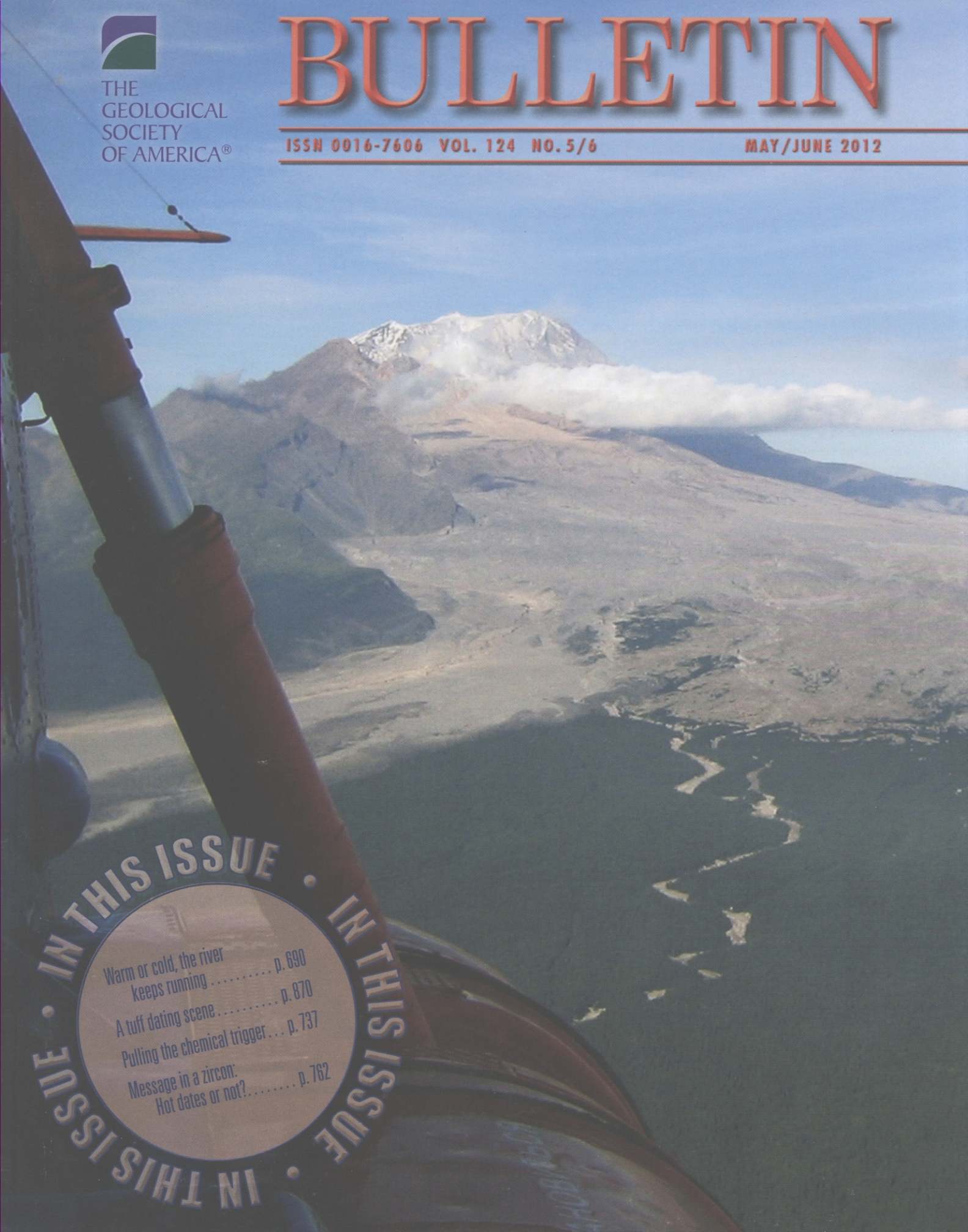

IN THIS ISSUE • IN THIS ISSUE • IN THIS ISSUE •

Surface textures and dynamics of the 2005 lava dome at Shiveluch volcano, Kamchatka

Michael S. Ramsey[1,†], Rick L. Wessels[2], and Steven W. Anderson[3]
[1]*Department of Geology and Planetary Science, University of Pittsburgh, 4107 O'Hara Street, Pittsburgh, Pennsylvania 15260, USA*
[2]*U.S. Geological Survey, Alaska Volcano Observatory, 4200 University Drive, Anchorage, Alaska 99508, USA*
[3]*The Mathematics and Science Teaching Institute (MAST) and Earth Sciences Department, University of Northern Colorado, Greeley, Colorado 80639, USA*

ABSTRACT

Shiveluch is one of the largest and most active andesitic volcanoes of the Kuril-Kamchatka arc. It commonly alternates between Vulcanian explosive eruptions and periods of dome growth and subsequent dome collapse–driven block-and-ash flows. The volcano was in an extended period of heightened activity for most of the period 2004–2010. We examined this activity in detail using thermal infrared (TIR) remote sensing as part of the urgent request protocol (URP) program of the Advanced Spaceborne Thermal Emission and Reflection Radiometer (ASTER) instrument and confirmed the results with ground-based photography and airborne TIR camera data. High-spatial-resolution TIR images were collected during both daytime and nighttime satellite overpasses prior to and following the large explosive event/eruption of 27 February 2005 and the dome growth that followed. During a field campaign in August 2005, a helicopter overflight designed to acquire visible and TIR data of the active dome was performed. This was a nadir-looking, low-altitude overflight and the first ever of Shiveluch volcano involving non-Russian scientists. The image data revealed an active crease structure in the center of the dome with a distinctly different, crescent-shaped, high-temperature (>380 °C) zone roughly perpendicular to the crease. In order to provide a time context and estimate extrusion rates, the airborne data were compared to the spaceborne ASTER data and long-distance ground-based photography of the dome acquired by our Russian colleagues. The presence of a crease structure and the complex thermal pattern on the surface were both unexpected discoveries that reveal the way in which exogenous dome growth was occurring at the time. This highly active period at Shiveluch provides a unique example to better understand silicic lava dome growth using TIR data. The results also demonstrate a straightforward approach for fusing ground, air, and spaceborne image data, which could be applied to other active domes around the world.

INTRODUCTION

The surfaces of recently emplaced silicic to intermediate lava domes are commonly destroyed by explosions or covered by younger lava lobes. However, subtle changes in the surface texture, composition, and/or temperature can signal new additions of lava, a change in the eruptive state, and/or the potential for further explosive activity (Anderson and Fink, 1990, 1992; Ramsey and Fink, 1999). Previous studies have shown that surface textures are a good indicator of the volatile distribution (and hence potential for explosive behavior) and internal structure of silicic lava domes (Fink and Manley, 1987; Fink et al., 1992; Anderson et al., 1995; Ramsey and Fink, 1999). Aerial photographs and ground-based sample collection of inactive flows and domes allow for a qualitative assessment of these textures, but such distinctions cannot be easily made for active domes due to changing conditions and safety concerns.

Although one of the most active volcanoes in the world, Shiveluch is infrequently visited and studied because of its remote location in northern Kamchatka, Russia, and the danger it poses to field-based researchers in close proximity. However, the variability in eruptive style and the threat it poses to aircraft routes in the North Pacific make Shiveluch an important target for quantitative monitoring. The Kamchatka Volcano Eruption Response Team (KVERT) and the Kamchatka Branch of Geophysical Surveys (KBGS) have monitored Shiveluch and the other active volcanoes in Kamchatka since 1993 (Kirianov et al., 2002; Neal et al., 2009). KVERT uses a combination of satellite and seismic monitoring as well as ground-based data collection (e.g., seismic, photography, web camera, geologic sample collection and mapping). In addition, daily satellite observations of Advanced Very High Resolution Radiometer (AVHRR) and Moderate Resolution Imaging Spectroradiometer (MODIS) data by both KVERT and the Alaska Volcano Observatory (AVO) are used to detect thermal anomalies and ash clouds, usually within hours after the onset of activity (Dehn et al., 2000). In 2005, frequent satellite data coverage combined with helicopter-supported aerial surveys and excellent field access allowed for unprecedented acquisition of high-resolution visual and thermal infrared (TIR) wavelength observations of the active andesitic lava dome at Shiveluch 5 mo after its largest explosive eruption in over 40 yr.

Thermal infrared data have been used in the past for temperature, composition, and thermophysical studies of geologic surfaces, including active volcanic targets. The TIR region is generally defined from 6 to 100 μm, although Earth's atmosphere limits that window to ~8–12 μm. Within this clear region, emitted energy from the surface can be accurately detected from ground-based, airborne, and satellite instruments. The emitted energy is a function of both the surface temperature (integrated over the area of the instrument's field of view) and the emissivity, which is related to the vibrational frequencies of the Al-Si-O and Ca-O bonds within the minerals. TIR remote sensing is therefore an excellent technique for the study of silicate and carbonate rocks (Lyon, 1965; Salisbury and Walter, 1989; Ramsey and Christensen, 1998; Ramsey and Fink, 1999).

In order to analyze the surface composition in a quantitative way, multiple spectral bands are

[†]E-mail: mramsey@pitt.edu

GSA Bulletin; May/June 2012; v. 124; no. 5/6; p. 678–689; doi: 10.1130/B30580.1; 8 figures.

required in the TIR region. Subtle mineralogical detection, large-scale compositional mapping, and determination of micron-scale textures can be made with increased spectral resolution of an instrument. For example, Ramsey et al. (1999) and Scheidt et al. (2011) used airborne and spaceborne (respectively) TIR data to map the mineralogical diversity and sediment source inputs in large eolian systems, and others have applied similar approaches to determine the composition of igneous and metamorphic rocks (Ruff, 1998; Feely and Christensen, 1999; Hamilton and Christensen, 2000; Wyatt and McSween, 2002).

If fewer spectral bands are available, TIR data are commonly used for surface temperature and thermophysical studies. For example, the pixel-integrated temperature has been used to determine the thermal inertia or the resistance to temperature change. Thermal inertia can be combined with other thermophysical modeling to make geological interpretations and determine the particle size and soil moisture of a surface (Gillespie and Kahle, 1977; Edgett and Christensen, 1991; Scheidt et al., 2010). The remote determination of temperature and its change over time are particularly important to active volcanic studies (Harris et al., 1997; Dehn et al., 2002; Wright et al., 2002; Ramsey and Dehn, 2004; Carter et al., 2008). However, combining airborne and spaceborne TIR data together to capture the various spatial and temporal scales of ongoing volcanic activity is not as common. This paper presents those data in combination with long-distance ground-based photography to capture the dynamic behavior of the lava dome at Shiveluch during this time period. These data sets of silicic lava domes have never before been acquired synergistically, and they show how similar observations are relevant to a better understanding of the changes in the appearance, extrusion rate, and thermal output of other active lava dome–forming volcanoes around the globe.

BACKGROUND

Shiveluch Volcano

Shiveluch volcano is located at 56.65°N, 161.36°E, and it is the northernmost volcano in the Kurile-Kamchatka arc (Fig. 1). It is the most active and one of the largest in Kamchatka, erupting several times per year on average (Fedotov and Masurenkov, 1991). Activity can range from andesite dome growth and Merapi-style collapse, to Vulcanian explosions that produce ash and gas clouds, to infrequent large explosive eruptions occurring every 100–300 yr on average. A 9-km-diameter south-facing summit caldera formed by a large eruption in the late Pleistocene is the center of current activity at Shiveluch (Ponomareva et al., 1998). The most recent large Plinian eruption occurred in 1964 and began with the formation of a large debris avalanche deposit that covers much of the unvegetated zone south of the volcano (Fig. 2).

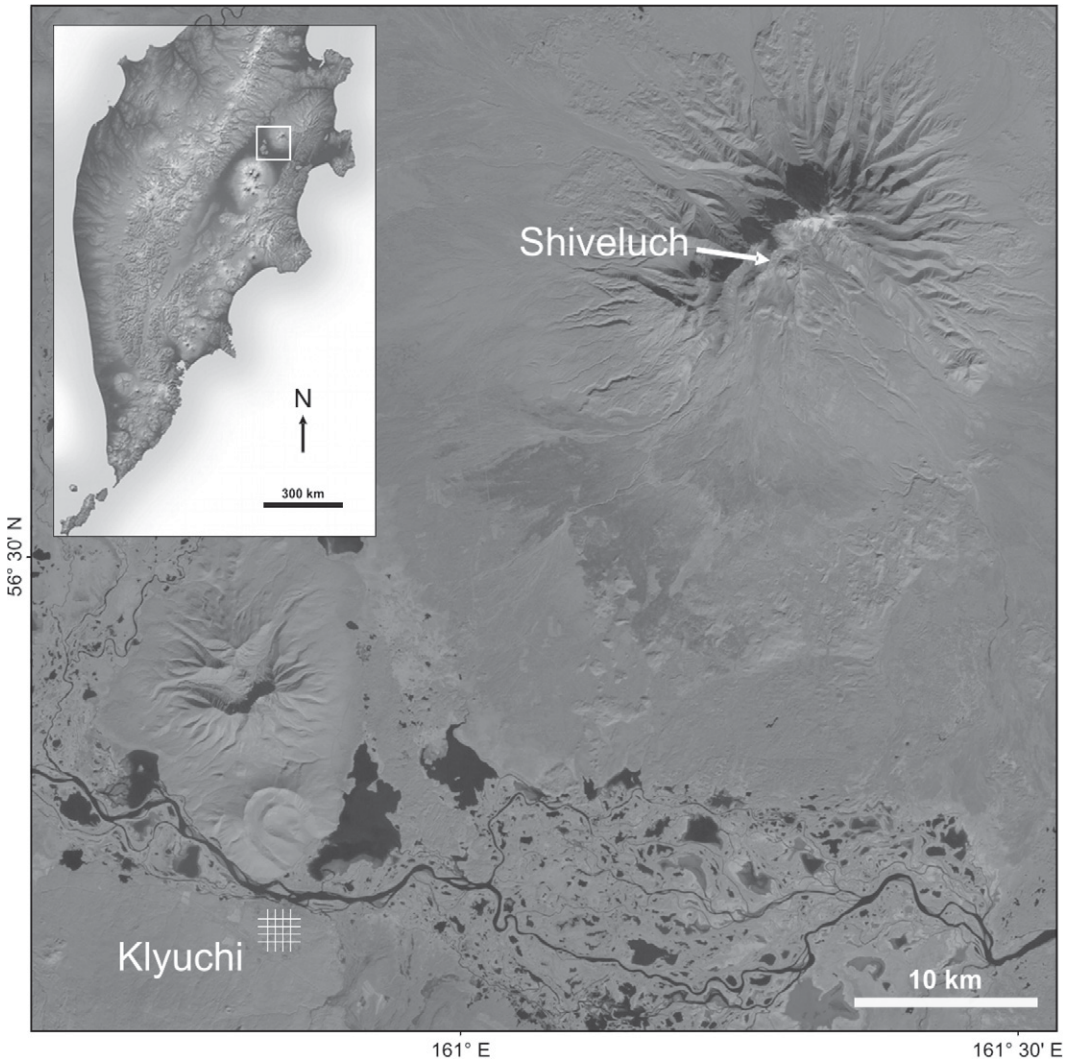

Figure 1. Landsat Enhanced Thematic Mapper Plus (ETM+) image acquired on 22 September 2000 showing the location of Shiveluch volcano and the surrounding area, including the village of Klyuchi (46 km southwest of the volcano). The map of the Kamchatka Peninsula is shown in the inset, and the white box indicates the area covered by the Landsat image.

Figure 2. Helicopter-based photograph looking north toward the summit of Shiveluch taken on 21 August 2005 by M. Ramsey. The older Stary Shiveluch is seen in the background with moderate snow cover, and the younger active dome complex of Molodoy Shiveluch is in the foreground. Debris avalanche and numerous smaller block-and-ash-flow deposits make up the unvegetated plain to the south of the breached, horseshoe-shaped summit caldera.

Within the last 10,000 yr, at least 13 of these catastrophic eruptions have occurred, producing distinct debris avalanche deposits to the south (Belousov, 1995; Ponomareva et al., 1998; Belousov et al., 1999).

Shiveluch is divided into the older, inactive construct (Stary Shiveluch) and the younger, active dome complex (Molodoy Shiveluch). The elevation varies from 3283 m above sea level (a.s.l.) at the older summit to ~2800 m at the currently active lava dome. Activity within the caldera is dominated by the near-continuous emplacement of multiple andesite lava domes/flows, subsequent collapse events and attendant block-and-ash flows, and interspersed larger eruptions that produce sustained vertical eruption columns and drifting ash clouds (Dirksen et al., 2006). This near-constant state of eruptive activity makes Shiveluch a high-priority target for hazard monitoring in the North Pacific region. Locally, ashfall can disrupt day-to-day activity in the villages within several hundred kilometers of the volcano. More importantly, drifting ash clouds commonly extend eastward over the Bering Sea and Pacific Ocean and into the routes of international passenger and cargo aircraft.

2005 Eruption

Beginning in May 2004, Shiveluch entered a continual state of unrest, producing intermittent explosive events, above-background-level seismicity, lava dome growth with associated collapse, and frequent ash clouds that drifted hundreds of kilometers to the east (BGVN, 2005a). An example of this unrest took place in the latter part of 2004 and continued into early 2005. An explosion on 6 September 2004 produced small pyroclastic flows and a 5.5-km-high ash plume. During 23–29 September, numerous shallow earthquakes up to M 2.3 were recorded (BGVN, 2005a). Explosive, ash-forming eruptions occurred on numerous occasions from September 2004 to February 2005. Soon after, thermal anomalies were detected with both low-spatial-resolution, high-temporal-resolution instruments such as AVHRR and MODIS, as well as high-spatial-resolution, lower-temporal-resolution instruments such as Advanced Spaceborne Thermal Emission and Reflection Radiometer (ASTER) and the Enhanced Thematic Mapper Plus (ETM+). The satellite data confirmed ground-based observations from KVERT and KBGS that a new lava dome was once again forming (McGimsey et al., 2007). This activity was typical behavior of the many months/years of activity at Shiveluch, and therefore did not indicate that a larger explosive event was imminent.

The 27 February 2005 explosive eruption produced the largest erupted volume at Shiveluch since the 1964 event. An ~24,800 km^2 pyroclastic flow deposit was emplaced, which was dominated by pumice and blocks of the old dome that extended to the south/southwest of the summit (BGVN, 2005a). This large deposit was hot enough to be recorded as a 45 pixel thermal anomaly in AVHRR data. Ash-fall was deposited in the villages of Klyuchi (46 km south) and Ust-Kamchatsk (250 km east). Ash clouds were detected extending more than 360 km over the western half of Kamchatka and the Pacific Ocean. Soon after this large eruption, new lava began to extrude at the summit caldera and continued throughout much of the remainder of 2005 (BGVN, 2005b). Prior to this eruption, the only local seismic station close to Shiveluch (SVL) was located ~8 km from the active vent. Unfortunately, the SVL station was destroyed by pyroclastic flows during the explosive event (Senyukov et al., 2009). The next closest station over the subsequent 8 mo was ~50 km from the volcano. However, seismicity from nearby Kliuchevskoi volcano dominated the seismograms from this station throughout much of 2005, revealing little about events at Shiveluch (Senyukov et al., 2009; Girina et al., 2007).

Despite the lack of seismic and deformation data, studies of the eruption deposits began almost immediately. The Russian Institute of Volcanology and Seismology (IVS) conducted a field reconnaissance of the deposit on 2 March 2005. The dome was not visited due to safety concerns. However, the temperatures, block sizes, and numerous photographs of the pyroclastic flow deposit were recorded (O. Girina, 2005, personal commun.). The large column-collapse–induced pyroclastic flow was mapped ~11.5 km to the southwest and another ~7.5 km to the west before terminating. Large (several meters in diameter) blocks of the lava dome were deposited over 10 km from the summit and attest to the energy of eruption and resulting pyroclastic flow.

The ASTER sensor was immediately targeted, and the first clear ASTER acquisition took place on 12 March 2005, after several earlier attempts failed to image the summit due to heavy clouds. The image was processed within 4 h of acquisition and found to contain the largest volcanic thermal anomaly by area ever detected by ASTER during the lifetime of the mission. The saturated pixels in ASTER Shortwave Infrared (SWIR) band 5 (2.17 μm) indicated the presence of hot material at the summit, but the pyroclastic flow deposit had already cooled below the SWIR detection threshold at that time of year and at the high northern latitude. However, ASTER TIR data still contained thermally elevated temperatures above the average background temperature over a month after the emplacement of the pyroclastic flow (Ramsey et al., 2008). ASTER data were acquired throughout the summer, including within a week of the field campaign. Unfortunately, due to a scheduling error, that overpass imaged the pyroclastic flow deposit but not the dome itself.

Thermal Infrared Data for Eruption Monitoring

Thermal infrared imaging of active volcanoes has become an increasingly important tool for monitoring and documenting dynamic volcanic

processes. In remote locations and/or in areas without the resources to deploy seismic and deformational monitoring instrumentation, commonly TIR remote sensing is the only quantitative tool available. Therefore, a quantitative understanding of its results in relation to the active volcanic processes is critical. Routine satellite-based monitoring by volcano observatories and other institutions typically occurs using low-spatial-resolution (kilometer-scale pixels), high-temporal-resolution (multiple images per day) TIR data from spaceborne sensors such as AVHRR, MODIS, Along Track Scanning Radiometer (ASTR), and Geostationary Operational Environmental Satellites (GOES) imager (Harris et al., 1997; Dehn et al., 2002; Wright and Flynn, 2003; Bailey et al., 2010). These data work well for detecting the large thermal changes that sometimes precede an eruption, as well as drifting ash clouds that commonly follow. However, higher-spatial-resolution data are required to detect the more subtle temperature changes and surface variability that are common during precursory unrest or ongoing extrusive activity. Satellite sensors such as ASTER and ETM+ provide this higher-spatial-resolution TIR data (e.g., tens of meters), although at much lower temporal resolution (e.g., days to weeks; Flynn et al., 2001; Ramsey and Dehn, 2004; Vaughan and Hook, 2006; Carter et al., 2008; Wessels et al., 2009). Airborne or ground-based thermal imaging cameras provide the highest spatial resolution (centimeters to meters) with a variable temporal resolution depending on the access and study design (Harris et al., 2005; Ball and Pinkerton, 2006; Rose and Ramsey, 2009; Schneider et al., 2009; Wessels et al., 2010). Combining high-resolution TIR from the ground with that from space can document precursory changes in existing thermal features as well as track deeper-seeded changes indicated by the development of new fumaroles, hot fractures, springs, and/or the melting of snow and ice (Calvari et al., 2005; Schneider et al., 2009; Wessels et al., 2010). These data can also be used to effectively observe passive/active SO_2 plumes (Watson et al., 2004; Bailey et al., 2010), to document lava dome and flow dynamics and effusion rates (Ramsey and Dehn, 2004; Harris et al., 2005), and to describe pyroclastic flow emplacement and the resulting deposits (Carter et al., 2007).

TIR data from spaceborne sensors have proven beneficial for describing the radiant temperature, surface composition, and passive SO_2 flux as well as changes in these properties at volcanoes over time (Pieri et al., 1990; Oppenheimer and Rothery, 1991; Harris et al., 1998; Watson et al., 2000; Wright et al., 2005). That information can be translated into heat flux and extrusion rate of the lava and gas emissions. This level of detail at the meter scale has only become possible with the spatial and spectral resolution of the ASTER TIR instrument. It is the first widely available commercial orbital TIR sensor with a spatial resolution better than 100 m/pixel that has more than two wavelength channels in that spectral region. ASTER was launched in December 1999 on the Terra satellite and measures the top of atmosphere radiance in 14 spectral channels (Yamaguchi et al., 1998). These are collected by three subsystems, each at a different spatial resolution: the visible and near-infrared (VNIR) sensor with three channels (0.56–0.81 μm) at 15 m spatial resolution, the short-wave infrared (SWIR) sensor with six channels (1.65–2.4 μm) at 30 m spatial resolution, and the TIR sensor with five channels (8.2–11.3 μm) at 90 m spatial resolution. Since April 2009, data from the SWIR sensor are no longer available due to a failed cooling system.

A program sponsored by the National Aeronautics and Space Administration (NASA) has been in place since 2004 to acquire better ground and spaceborne VNIR and TIR data of the volcanoes in Russia and Alaska (Ramsey and Dehn, 2004; Carter et al., 2007, 2008; Rose and Ramsey, 2009; Duda et al., 2009). The urgent request protocol (URP) program automates the ASTER sensor's ability for targeted observations using data from higher temporal sensors (i.e., AVHRR) as a scheduling trigger in a sensor-web concept. The URP program allows data acquisition frequency as high as night-day-night observational triplets approximately every 3 to 4 wk and day-night pairs approximately every 7 to 10 d during periods of high eruptive activity for volcanoes in Kamchatka. Once received from the sensor, the data are automatically processed, staged, and made available to the URP program scientists, KVERT, and AVO. The ongoing multi-agency research and operational collaboration have proven highly successful, facilitating faster data availability and improved situational awareness during eruptions in the North Pacific region. The availability of frequent data is also critical in order to record rapid changes in activity and to compensate for the obscuration by heavy/recurring cloud cover.

As of mid-2011, over 110,000 individual ASTER scenes have been collected for Earth's ~1000 most active volcanoes, averaging ~5 daytime and 6 nighttime scenes per volcano per year. For Shiveluch, the average is much higher: 13 daytime and 17 nighttime images per year or at least one ASTER image of the volcano every 12 d on average (Carter and Ramsey, 2010). The higher temporal frequency of ASTER for volcanoes in Kamchatka has been facilitated by the closely spaced satellite overpasses at high latitudes and specific data acquisition programs such as the URP (Ramsey et al., 2004; Duda et al., 2009).

METHODOLOGY

Ground-Based Photography

In addition to the regular satellite observations of Shiveluch analyzed by KVERT and AVO, long-distance ground-based photography and web camera observations have been used for many years to document ash plumes and monitor changes in the dome position and its linear growth rate (Fig. 3). Ground-based photography is conducted from the village of Klyuchi and provides a relatively straightforward means by which to monitor changes in the dome over time and to calculate the linear growth rates in m/d (Girina et al., 2004). These rates and documented changes provide the best calibration source for satellite and airborne observations. However, clouds commonly obscure the dome complex during extended periods of the year, which makes a consistent time series difficult to produce. Therefore, the ability to provide regular and more quantitative observations of the dynamic dome growth, using, for example, TIR observations from space, is critically important.

2005 Field Campaign

Plans were made for a field campaign in August 2005 in order to validate the ASTER data, acquire air- and ground-based thermal imaging of the new dome and pyroclastic flow deposits, and to collect samples where possible. Previous collaboration among researchers at the University of Pittsburgh, AVO, and IVS provided rapid logistical access for travel and allowed the field team to access Shiveluch, which is normally very difficult because of the remoteness of the volcano and the danger due to the near-constant activity. During the 2 wk field campaign in August 2005, nearby recently active Bezymianny and Kliuchevskoi volcanoes were also visited and sampled (Carter et al., 2008; Rose and Ramsey, 2009).

Data and geologic samples collected at Shiveluch during the field campaign provided observational validation for the satellite analyses. This information also allowed landscape changes over the previous 5 mo to be described. In particular, this work enabled a quantitative analysis of the new pyroclastic flow deposit's surface textures and temperatures to be described (Ramsey et al., 2008). Simultaneous TIR camera data, digital visible photographs/video, and global positioning system (GPS)

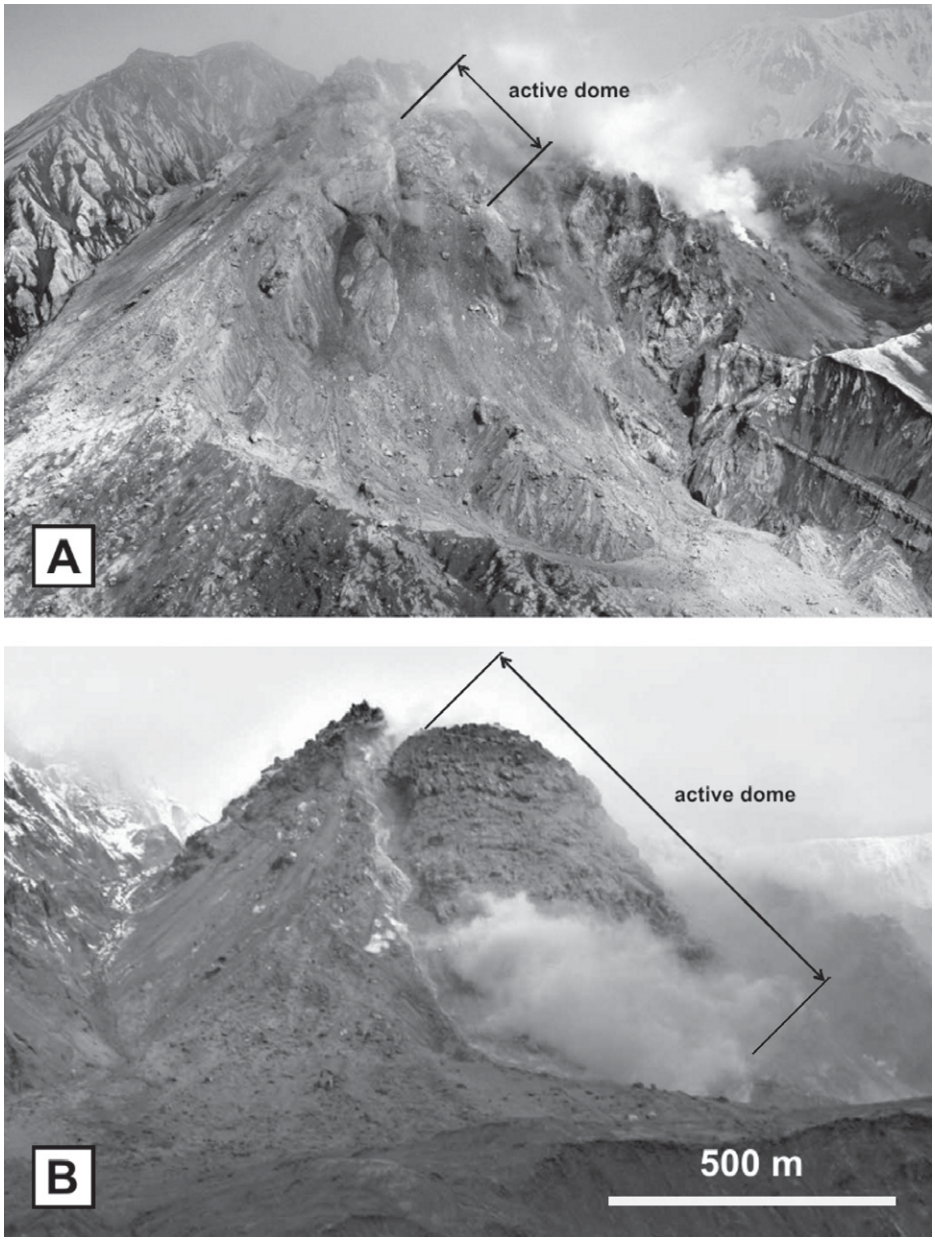

Figure 3. Ground-based photographs of the Shiveluch lava dome complex following the 10 May 2004 eruption (courtesy of Y. Demyanchuk, Russian Institute of Volcanology and Seismology [IVS]). The images were used here to document a linear growth rate of 4–6 m/d of the new lava dome. (A) 21 May 2004. (B) 28 July 2004.

data were acquired during multiple helicopter overflights of both the pyroclastic flow deposits and the active summit dome. The altitude of each flight varied from 500 to 800 m above ground level (AGL), and a port in the floor of the helicopter allowed nadir imaging using the handheld TIR and visible cameras. Additional oblique photographs and video were also acquired during the flights.

During the helicopter overflights of Shiveluch in 2005, the TIR imaging system was a handheld FLIR ThermaCAM S40 infrared camera. The camera utilizes a 320 by 240 microbolometer detector array that is sensitive from 7.5 to 13 µm to convert TIR-emitted radiance from the surface and atmosphere into calibrated brightness temperature. The system has an integrated 24° lens with an instantaneous field of view (IFOV) of 1.3 mrad, which produced a pixel resolution of the dome's surface of 1.04 m from an elevation of 800 m above. This resolution improved to 0.65 m/pixel at 500 m elevation above the surface. The S40 camera has a noise equivalent delta temperature (NEΔT) of 0.08 °C at 30 °C and an accuracy of ±2 °C (±2%). The data can be acquired in three temperature ranges: –40 to 120 °C, 0 to 500 °C, and 350 to 1500 °C to prevent saturation. Data were acquired either in a single-image mode, storing the data to an internal compact flash card, or at high frame rates between 15 and 30 Hz using a Firewire connection to a laptop computer for storage. One advantage of the high frame rate is that features on the ground are highly oversampled, and therefore frames with image blur due to helicopter or human movement could be discarded without the loss of surface coverage.

The total radiant energy (L_t) measured by the FLIR camera is a combination of the energy emitted/reflected from the surface as well as the energy emitted and scattered by the intervening atmosphere. It can be described simply by:

$$L_t = \varepsilon_s \tau_a L_s + (1 - \varepsilon_s)\tau_a L_r + (1 - \tau_a)L_a, \quad (1)$$

where ε_s is the emissivity of the surface, τ_a is the atmospheric transmission, L_s is the radiant emission from the surface, L_r is the reflected emission onto the surface from nearby sources (including the sky), and L_a is the direct emission from the atmosphere into the field of view of the camera. The camera measures L_t and converts this energy to a temperature for each pixel using a series of internal calibration coefficients and data input by the user. A first-order correction for the atmospheric emission and transmission terms is made by measuring the distance to target, ambient air temperature, and relative humidity. A broadband average emissivity of the surface is assumed (typically between 0.96 and 1.0 for most silicate rocks). Air temperature and humidity were measured during each overflight. The distance to target was calculated from the difference between the time-synchronized GPS helicopter position and the estimated position of the feature being imaged. Clear, nonblurred TIR image frames were later extracted from the FLIR video files, composited together using the FLIR ThermaCAM Researcher software, and draped over the corresponding high-resolution visible camera images in order to correlate the thermal distribution on the surface with the visible morphology. The color scale for the FLIR images represents a linear scaling for 98% of the data and not the full temperature range.

In addition, aerial photographs and video (both nadir and oblique) were acquired simultaneously for comparison with the TIR data. Because the size of the FLIR pixels could be precisely determined, the higher-resolution visible images could also be scaled by comparing geomorphic features in each data set. This

allowed the dome, individual blocks, and the central crease structure to be measured accurately to within 50 cm.

ASTER Data Analysis

In order to document changes from the early and later phases of dome emplacement, the FLIR and ground-based photography were compared to two ASTER images acquired within 1 mo of the February eruption. Changes in the size, extrusion rate, and location of the maximum temperature of the dome in each TIR image were calculated. The ASTER TIR data were derived from the calibrated, at-sensor (level 1B) radiance data. These data were first corrected for atmospheric absorption/emission using the standard approach for ASTER, with specific corrections for the image location and the time of year of acquisition (Thome et al., 1998). In order to extract accurate pixel-integrated brightness temperature and emissivity data from the atmospherically corrected radiance data, the downwelling sky radiance reflected off the surface must also be removed. This is accomplished using an iterative approach, which separates the brightness temperature and emissivity for each pixel using the temperature-emissivity separation (TES) approach (Gillespie et al., 1998). The processed (level 2) surface temperature and surface emissivity data products are distributed by the NASA Land Processes Distributed Active Archive Center (LP DAAC).

ASTER TIR radiance data can be directly impacted by the magnitude and distribution of surface temperatures in each pixel. For example, hot areas on active lava flows are typically smaller than the area covered by a 90 m TIR pixel. As a result, the radiance measured is an area-weighted sum of the multiple-subpixel radiating components (Wright and Flynn, 2003). Depending on the range of temperature differences in a given pixel, this averaging can produce large underestimation of the actual high-temperature components and major errors in the derived surface emissivity (Rose and Ramsey, 2009; Rose et al., 2010). These pixels are easily identified by a significant decrease in the slope of the emissivity spectra at longer wavelengths, which can be corrected using data from other wavelength regions (e.g., the SWIR and VNIR). Temperatures derived from these mixed radiance data are therefore commonly denoted as pixel-integrated temperatures. For ASTER TIR data, saturation of the pixels occurs where the detected radiance becomes large enough to exceed a value corresponding to a pixel-integrated brightness temperature of ~97 °C. In these situations, useful data can be extracted using the at-sensor radiance from the higher-spatial-resolution SWIR channels, which are sensitive to pixel-integrated brightness temperatures from 100 °C to 467 °C (Urai et al., 1999; Rose and Ramsey, 2009).

The first clear ASTER daytime scene acquired on 12 March 2005 was followed 17 d later by the first clear nighttime data on 29 March 2005 (22:50:08 local time). The daytime scene contained VNIR, SWIR, and TIR data, and as is typical for ASTER nighttime acquisitions, the 29 March scene only contained SWIR and TIR data. These ASTER URP data sets were initially analyzed within 4 h of acquisition, and the information was shared with AVO and KVERT. The images were precisely georeferenced, and the number of significantly anomalous SWIR and TIR pixels was summed to assess the size of the dome and its linear growth rate from 12 March to 29 March. The same process was used to compare the 29 March data with the FLIR TIR data acquired in the field on 21 August (146 d later). Specifically, the higher-spatial-resolution SWIR data were used to identify pixels with pixel-integrated temperatures >300 °C, which were likely locations of active lava extrusion or lobe collapse on the dome. The TIR data were used to assess the overall dome size/temperature as well as the pyroclastic flow deposit characteristics. Movement of the hottest pixel in the TIR data sets, which in most cases represents the talus-producing flow front of the growing dome, was used to estimate the dome growth direction and rate. This information was then compared to the values reported by KVERT using the long-distance ground-based photography. Because of the lack of any other geophysical data sets, the ground-based photography provided the only other independent data for comparison to the TIR data.

RESULTS

Ground-Based Photography

The new dome was initially detected using long-distance photographic surveys conducted by IVS/KVERT. It appeared a week after the large eruption and continued to grow episodically throughout the following months (Fig. 3). The photographic observations do not allow for a precise eruption rate estimate (in m^3/d) or volumetric change (in m^3) of the dome because the photographs are taken from a single vantage point. The average linear growth rate reported by IVS/KVERT was 4–5 m/d (Girina et al., 2004).

The February 2005 eruption demolished the preexisting 2004 dome, which had represented its largest volume since August 1980. The new dome was emplaced in the northwest quadrant of the caldera, which is the same locations as dome extrusions from 2001 to 2004 (Zharinov and Demyanchuk, 2008). The lava dome continued to grow during the month of March, interspersed with several episodes of ash-and-gas plumes that rose to a maximum of ~2.8 km above the dome (BGVN, 2005b). Observations from April 2005 confirmed the position and relatively small size of the dome (Fig. 4A). Throughout April and May, the vent migrated west and south, and that portion of the dome grew dramatically, failing several times to form block-and-ash flows (BGVN, 2005b). This movement of the eruptive center of the dome was also confirmed in later observations (Zharinov and Demyanchuk, 2008). The flows continued during June and July, were large at times, and corresponded with a change in extrusion direction of the dome to the south, where it progressed over a slope and became more prone to failures at the leading edge of the dome. On 15 July, an ash cloud accompanying a dome collapse spread more than 700 km to the west, reaching the Sea of Okhotsk (BGVN, 2005c). Long-distance photography acquired on 8 August 2005 prior to the field campaign confirmed the change of extrusion direction and increasing size of the dome (Fig. 4B).

Airborne FLIR/Visible Observations

The overflight of Shiveluch's active dome took place on 21 August 2005 and consisted of two north-south passes at ~500 m and 800 m above the Molodoy Shiveluch caldera. The most noticeable feature in the visible camera/video data (Fig. 5) was the presence of a blocky, active lava dome bisected by a single dominant crease structure (Anderson and Fink, 1992). Large smooth blocks flanked the crease, with the remainder of the dome consisting of a more scoriaceous texture. This textural distribution was identical to that reported by Anderson and Fink (1990) for the dacitic lava emplaced on the growing dome during the 1980–86 Mount St. Helens eruption (Fig. 6). The Shiveluch dome was nearly circular in plan, roughly cylindrical in cross section, and located in the sloping southern quadrant of the caldera. Dome rock from earlier stages of emplacement encircled newer dome material on the west, north, and east flanks (Fig. 3). Small fumaroles and diffuse areas of fume were seen in the caldera to the north of the dome. The higher-spatial-resolution visible camera images from the overflight were scaled to the FLIR data, and the new dome was calculated to be 335 m by 410 m in diameter, with a height of 32 m (determined from the shadow length and solar angle). The volume of the new dome at the time of the

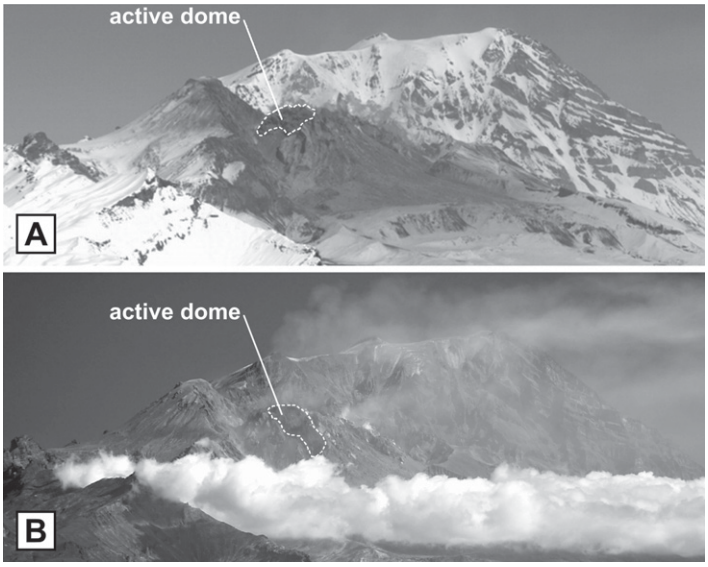

Figure 4. Changes in the size and position of the Shiveluch lava dome following the February 2005 eruption (courtesy of Y. Demyanchuk, Russian Institute of Volcanology and Seismology [IVS]). (A) 26 April 2005. (B) 8 August 2005. The dome and the center of extrusion/direction of lobe development have migrated to the south (toward the camera) over time similar to what was seen in the thermal infrared data (see Fig. 7C). Images are approximately 10 km wide.

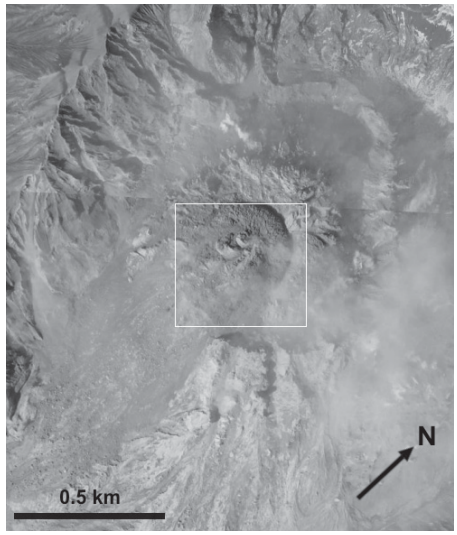

Figure 5. Nadir-view visible wavelength photograph mosaic of the Shiveluch lava dome taken on 21 August 2005, ~800 m above the caldera. The newest dome rock is darker with a scoriaceous texture, and a prominent central crease structure is oriented approximately north-south. White rectangle denotes the area shown in Figure 8.

data collection (calculated using the volume of a cylinder with an average radius of 187 m) was ~$3.5 \pm 0.8 \times 10^6$ m^3.

Individual images with no motion blur were extracted from the high-speed FLIR video files and used to create a mosaic base from which to geolocate the visible images. The data were first corrected for atmosphere and look angle through input of the air temperature, relative humidity, and angular distance of the camera above the dome, as well as an estimation of the broadband emissivity of the dome rocks. The atmospheric and positional data were measured separately during the overflight, and the broadband emissivity value (ε_{max} = 0.97) was used based upon laboratory emissivity data of samples collected in the field. The combined VIS- TIR airborne fused data set was then georeferenced to the ASTER VNIR image acquired on 29 March 2005 in order to have one calibrated, scaled, and geolocated data set in all wavelength and spatial scales for the analysis (Fig. 7A).

The FLIR data over the lava dome had a temperature range from –5 °C to 405 °C, with the maximum scene temperature located in the northernmost axial valley of the crease structure (Fig. 7B). Much of the rest of the dome's carapace was cool (at or below the average background temperature of 22 °C). However, two other thermally elevated zones were detected away from the active crease structure. The first zone was nearly as hot as the crease itself and was located at the southernmost region of the caldera in the area of downslope dome spreading and active rockfall from the active lobe. The second zone was a triangularly shaped area of fumaroles northeast of the dome at the base of caldera rim, which was cooler but still elevated above the background temperature. In addition, a thin thermal anomaly was also detected extending from the northern tip of the crease structure on the dome, through older dome rock, toward the second warm zone (Fig. 7B). It continued northeast, eventually intersecting the fumarole field. This thin anomaly marks a series of fractures that parallel the larger-scale tectonic orientation (NE-SW) in the region. It is likely that this orientation influences the vent geometry and hence the morphology of the caldera and overall emplacement of the dome.

Interestingly, the temperature distribution on the dome surface was neither symmetrical about the dome itself nor the crease structure. A crescentic thermal boundary existed on the active dome between cooler rock to the north and hotter material to the south (Fig. 7B). This boundary pointed in the downslope direction of dome growth and intersected the northern extent of the crease structure, the hottest area detected in the FLIR data. The boundary was most likely an incipient detachment surface that delineated a secondary active spreading zone (in addition to the lateral extrusion of lava in the crease) that was controlled by the topography of the caldera floor. Within the crease structure, the thermal gradient from the crease floor to the tip of the large smooth slabs was only 2.8 ± 0.3 °C/m, indicating that very little cooling had occurred and that slab extrusion from the crease was active at the time of image capture. Therefore, during the time of the overflight, there was exogenous dome growth occurring laterally in the crease at the same time that the dome was growing in the downslope direction.

ASTER Data Analysis

Several of the initial ASTER images of the caldera and dome complex were selected to compare the growth and movement of dome immediately following the eruption as well as months later following the aerial FLIR data captured in August 2005. The clear daytime (12 March 2005) and nighttime scenes (29 March 2005) were used for this analysis. The L2 TIR kinetic temperature image for 12 March had four TIR pixels (32,400 m^2) that were thermally elevated to a significant degree (>70 °C). This number increased to 11 TIR pixels (89,100 m^2) 17.5 d later, which was used as a proxy for the growth rate, calculated to be 3.2×10^3 m^2/d. The hottest pixel in each scene was also identified and assumed to be the location of

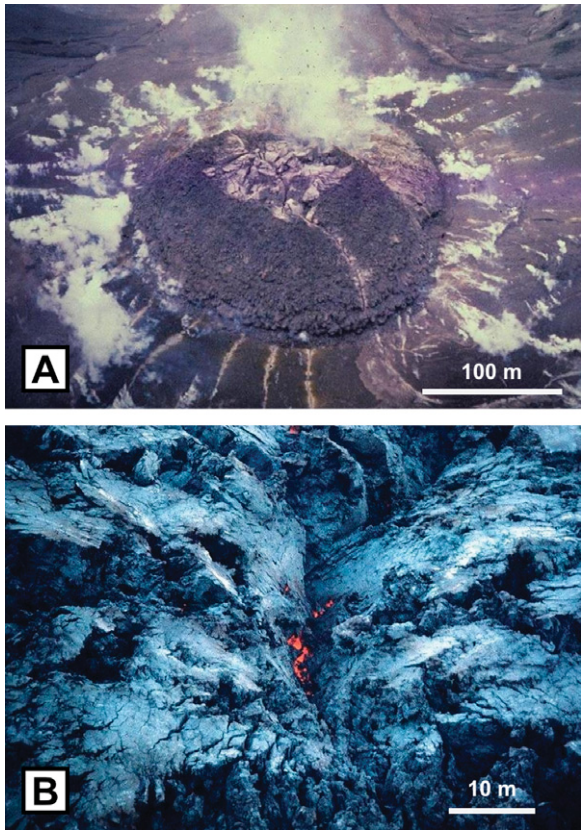

Figure 6. Mount St. Helens lava dome showing both scoriaceous and smooth lava textures with a central crease structure (photographs courtesy of the U.S. Geological Survey). (A) December 1980 southeast lobe. (B) Close-up view of the crease structure of the same lobe taken earlier than photo in A. Incandescent lava can be seen at the base of the crease valley.

the flow margin, where frequent rockfalls would expose hot interior material. The distance between the hottest pixels in the two March scenes was 108 m, resulting in a linear growth rate of 6.2 ± 0.3 m/d. If the maximum thickness of the dome is assumed to be approximately equal to that observed in August (32 m), then the upper bounds on change in the volume of the dome could be calculated to be from 1.04×10^6 m^3 to 2.85×10^6 m^3 in 17.5 d (a rate of 1.2 m^3/s). However, based on the past behavior of the dome at Shiveluch, it is likely that the extrusion rate was higher and some of the extruded material was being removed by small explosions and dome collapse events as the dome grew larger.

In order to compare the temperature and extrusion rate of the dome immediately after the large eruption to similar values later in the year, the ASTER TIR data from March were superimposed on the geolocated FLIR data from August (Fig. 7C). As in the previous comparison, the position of the hottest pixel was assumed either to be the location of new exogenous material or the active dome front where rockfall was exposing hot material. In either case, the movement of this position can be used as a proxy for the linear growth of the dome. During the 146 d from the ASTER TIR to the FLIR acquisition, the hottest pixel tracked 510 m ± 45 m to the southeast, resulting in an average advance rate of 3.5 ± 0.3 m/d. This growth direction is consistent with the ground-based field photography, which showed that the dome initially began to extrude in the northwest portion of the caldera and later progressed south, eventually extending over the southern flank (Fig. 4). However, this linear growth rate is somewhat less than that derived from either the earlier photographic measurements or from the earlier ASTER data in March (i.e., 4–6 m/d), indicating a slowing of dome growth in the subsequent months. Even with this slower linear growth rate, the volume of the dome continued to increase from an estimated 2.85×10^6 m^3 to 3.50×10^6 m^3 from March to August, indicating that lava continued to be added to the dome, likely by a combination of exogenous (i.e., the crease structure) and endogenous growth during this time period.

DISCUSSION

The long-distance images collected by KVERT in 2004 and 2005 following the two large eruptions reveal new dome growth commencing within days to weeks. With the destruction of the only local seismic station following the 2005 eruption, these photographs typically would provide the only long-term record of dome extrusion rates. The average linear growth rate for the weeks following the 2005 eruption was calculated to be 4–5 m/d using this technique. This growth and movement of the dome's position were also detected by examining geolocated ASTER data sets over the same time period. By comparison, using ASTER images acquired 17.5 d apart in March 2005, the linear growth rate was calculated to be 6.2 m/d. The direction of the flow front, as indicated by tracking the hottest pixel(s) in the TIR data, progressed from north to south, with the dome eventually flowing over steeper topography and collapsing to produce block-and-ash flows (Fig. 4). The rate calculated from the ASTER data decreased to 3.5 m/d from 29 March to 21 August 2005. These values are likely more accurate than the ground-based photographic measurements because the entire dome was imaged by the TIR data. The variability is also expected because many active lava domes experience episodic growth (e.g., Swanson et al., 1987; Rose, 1987).

If the dome thickness is assumed to be similar to that measured in August (32 m) over the months following the 2005 eruption, the volume increased from an estimated 1.04×10^6 m^3 to 2.85×10^6 m^3 to 3.50×10^6 m^3 from 12 March to 29 March to 21 August. This translates to a decreasing extrusion rate from an average of 1.2 m^3/s in March to 0.05 m^3/s between March and August. These values are on the low side of the extrusion rate range calculated from other silicic lava domes, such as 0.6–1.9 m^3/s for the 1922 to present Santiaguito dome (Rose, 1987), 1.4–40.3 m^3/s for the 1980–1986 Mount St. Helens dome (Anderson and Fink, 1990), and 2.2–35 m^3/s for the final 2009 Redoubt volcano dome (Diefenbach et al., 2012). However, the extrusion rates calculated for Shiveluch should be considered minimum estimates because it is likely that some amount of dome material was also being removed during explosive and collapse events between March and August. Therefore, it would be unlikely for the dome to have maintained a constant thickness and rate of growth over that time period.

Another approach exists to estimate lava extrusion rates using thermal cooling models and TIR data from sensors with low spatial resolutions (e.g., 1–10 km). This has been done by deriving a simple heat budget in which all heat supplied to the lava flow is lost from the flow surfaces by way of convective and radiative heat transfer (Pieri and Baloga, 1986; Crisp and Baloga, 1990; Harris and Stevenson, 1997; Harris et al., 2007). Estimating the volume flux necessary to account for cooling will yield time-averaged discharge rate (Wright et al., 2001). Application of this satellite-based technique has been demonstrated to correlate well with independent methods for estimating lava flow

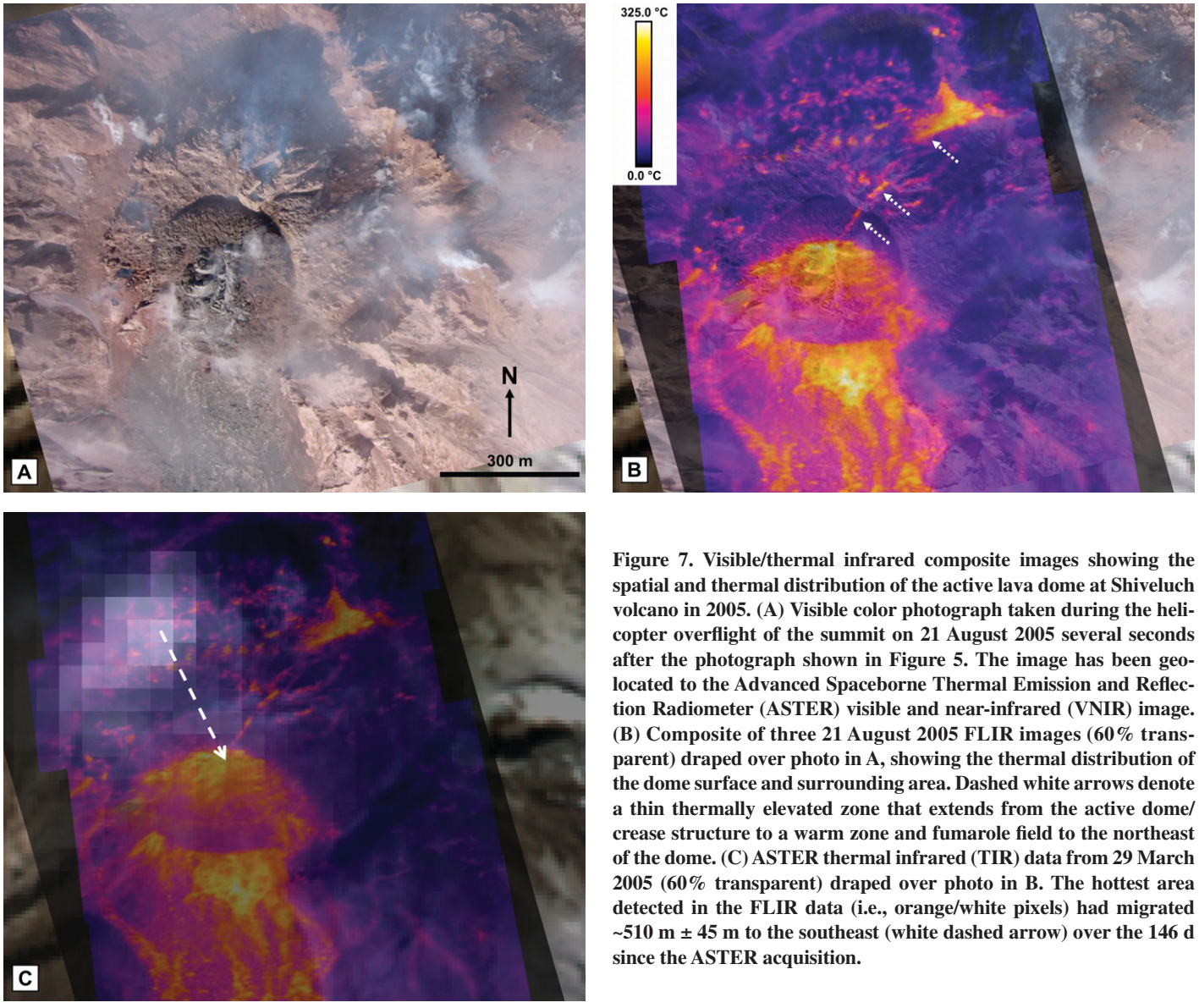

Figure 7. Visible/thermal infrared composite images showing the spatial and thermal distribution of the active lava dome at Shiveluch volcano in 2005. (A) Visible color photograph taken during the helicopter overflight of the summit on 21 August 2005 several seconds after the photograph shown in Figure 5. The image has been geolocated to the Advanced Spaceborne Thermal Emission and Reflection Radiometer (ASTER) visible and near-infrared (VNIR) image. (B) Composite of three 21 August 2005 FLIR images (60% transparent) draped over photo in A, showing the thermal distribution of the dome surface and surrounding area. Dashed white arrows denote a thin thermally elevated zone that extends from the active dome/crease structure to a warm zone and fumarole field to the northeast of the dome. (C) ASTER thermal infrared (TIR) data from 29 March 2005 (60% transparent) draped over photo in B. The hottest area detected in the FLIR data (i.e., orange/white pixels) had migrated ~510 m ± 45 m to the southeast (white dashed arrow) over the 146 d since the ASTER acquisition.

extrusion rates at many volcanoes (Harris et al., 2007). However, the combination of a mostly cooled carapace, endogenous and exogenous dome growth, and the frequent rockfalls at Shiveluch would produce a large underestimate of lava flux using this approach. The radiant heat flux values derived from lava crusts with a strong flow-front thermal signature and/or near-background crust temperature introduce significant error and variability in derived extrusion rate values.

Crease structures in domes over the vent area typically expose smooth, dense lava from the flow interior, creating a dome with the distinct textural progression from smooth to scoriaceous (Fig. 6A). Lava immediately below smooth crease structure walls is able to remain hot beneath the dense crust, eventually breaking through as the smooth walls move outward from the central valley of the crease (Fig. 6B). The ability of this dense material to retain heat as it moves outward allows underlying material to remain hot and plastic enough for vesiculation to occur, and this is reflected in the low thermal gradient measured outward from the central valley (Anderson and Fink, 1992). Once the vesicular material breaks through the smooth walls and is exposed at the surface, heat loss is increased through the greater surface area provided by the scoriaceous carapace, thus explaining the low overall temperatures observed in areas away from the active crease.

The formation of a crease near the summit of the dome and the creation of a predominantly scoriaceous surface texture away from the crease provide clues to the surface stress regime of the dome and degassing processes occurring during its formation (Fig. 8). Crease structures emplaced during the 1980–1986 eruption of Mount St. Helens formed either on lobes situated on the relatively flat crater floor, or on the flat summit portion of lobes on steeper slopes (Anderson and Fink, 1992). Anderson and Fink (1992) suggested that a tensional stress regime was required for crease structure formation, and it would occur if the surface crust of the flow could spread laterally. At Shiveluch, Figure 3B shows a relatively flat dome summit area approaching nearly 200 m across, sufficient to form a large crease structure.

The predominantly scoriaceous carapace that formed on the remainder of the Shiveluch dome is similar to that found during the first 2 yr of the 1980–1986 Mount St. Helens dome and the

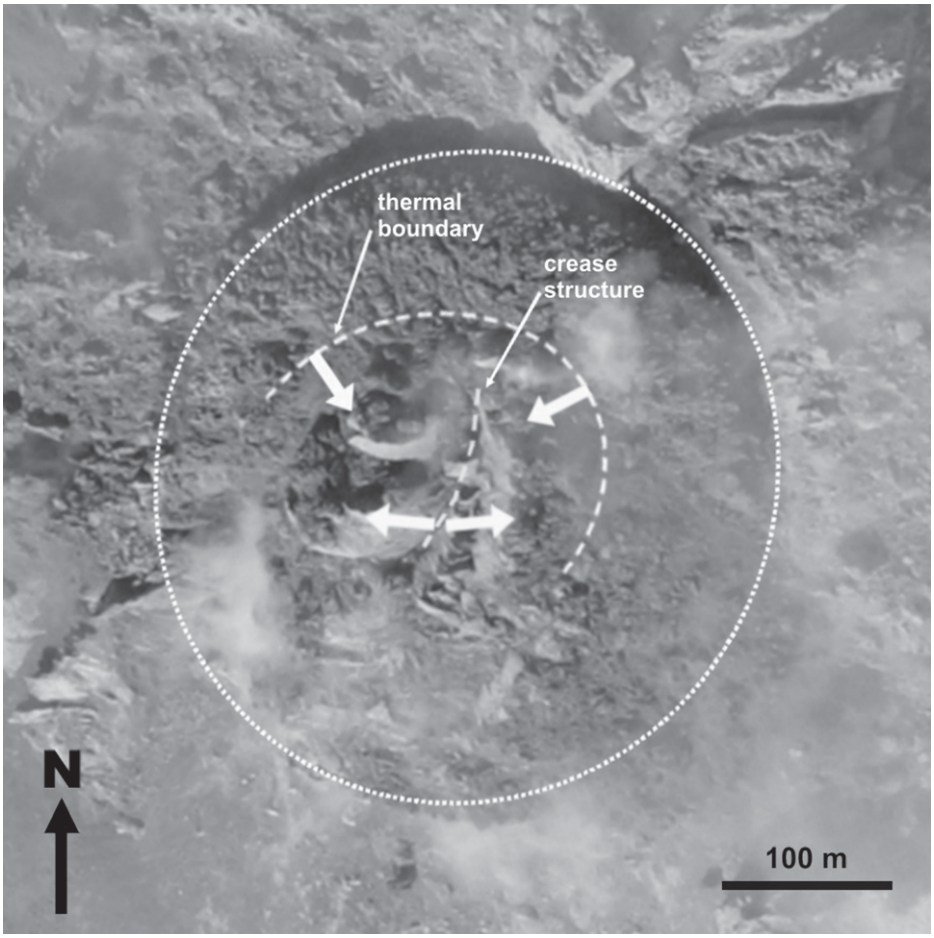

Figure 8. Highest-resolution photograph of the active 2005 lava dome and crease structure (extent of the active dome noted by the dotted white circle). The spreading crease structure is the main structural feature in the growing dome. The asymmetric thermal boundary, detected only with the FLIR data, is also noted and is most likely a detachment surface of active dome growth, but it could also have been a fracture formed when growth of the dome encountered a steeper slope to the south. The solid white arrows denote the most likely growth direction of the active dome.

2009 Redoubt dome. During the final 2 yr, lobes of the Mount St. Helens dome displayed very little scoriaceous textures, being dominated by smooth lobes. Anderson and Fink (1990) suggested that during the first 2 yr, the relatively small dome provided little resistance to lava moving to the surface, allowing new material to arrive at the surface in a fairly gas-rich state, thus leading to vesiculation near or at the surface (i.e., faster extrusion rates correlate with more scoriaceous textures). As the dome grew and its surface strengthened, the amount of endogenous growth that occurred before lobe extrusion increased dramatically (Fink at al., 1992), allowing new material rising toward the surface to more thoroughly degas, limiting surface vesiculation, and forming denser/smoother lava (Anderson and Fink, 1990). At Shiveluch, the young, small, and predominantly scoriaceous surface suggests that the dome itself was providing little resistance to new lava emplacement and vesiculation at the time of the overflight 6 mo after the large eruption.

CONCLUSIONS

Although this study focused on the analysis of one large eruption at Shiveluch, the methodology could be exported to any dome-forming volcano. The use of ASTER only or a combination of ASTER plus FLIR TIR data has been shown to be a valid and promising approach to dome monitoring where other TIR-based techniques would be far less effective. In addition to the broader approach, this work presented data from the first-ever FLIR overflight of the active dome at Shiveluch volcano. These data detected an actively forming crease structure on the new dome as well as resolved the thermal distribution of the dome and other features within the caldera. By comparing the high-spatial-resolution FLIR data to the lower-resolution ASTER TIR data collected 146 d prior, it was possible to describe the changes in the size, morphology, and position of the active vent area. The average linear growth rate of the dome in the early phase of the eruption was calculated to be 6.2 m/d by tracking the movement of the hottest ASTER pixel. This rate decreased to 3.5 m/d in the later phases, and both of these rates compare well to the 4–5 m/d rate calculated by long-range digital photography of the dome, which represented the only other independent data available following the large explosive blast.

Ground-based monitoring of silicic lava dome growth on active volcanoes can be dangerous; however, the data collected are critical to determine the future hazard potential. Long-distance visual photographic observations are one way to accomplish this monitoring in a relatively safe way, but they become impossible in times of poor weather, at night, and during vigorous eruptive activity. Furthermore, these images have limited views and would not work well on volcanoes with partially obstructed views of the growing dome. The airborne data are more expensive to acquire and subject the team to higher risks; however, these data provide a planimetric complement to the oblique photography. Similar data from space have a poorer spatial resolution, but they can be acquired regularly and provide additional wavelengths for more accurate temperature, compositional, and textural analysis (Ramsey and Dehn, 2004; Vaughan et al., 2005; Carter and Ramsey, 2009). Currently, this high-temporal-frequency, high-spatial-resolution data acquisition is only possible over short time intervals with the ASTER URP program in the North Pacific region (Duda et al., 2009; Carter and Ramsey, 2010). However, it is now being expanded worldwide using alerts from the MODVOLC program (Wright et al., 2002).

The use of high spatial/temporal TIR data from space to estimate the thermal flux and extrusion rate of the silicic lava dome at Shiveluch compares well with more traditional methods. It also provides a complementary monitoring and forecasting tool to ground-based methods such as seismic and deformation measurements when they are available. However, for such data to be useful for both scientific analysis and more accurate monitoring, as well as limiting the impact of poor weather conditions, the temporal resolution must be more frequent than even the URP-augmented ASTER data can provide. Future TIR sensor development should focus on improvements in both spatial and temporal resolution to make this type of volcanic monitoring

and science a possibility. For example, the future Hyperspectral Infrared Imager (HyspIRI) is proposed to have increased capabilities from that of ASTER (e.g., 60 m/pixel spatial resolution, eight spectral bands, and 1 d temporal resolution over the volcanoes in the northern latitudes) (NRC, 2007). If integrated into a rapid response system using other data sets, such an instrument could provide daily, detailed data of disruptive and hazardous eruptions. High-spatial-resolution and high-spectral-resolution TIR data would bridge the gap between sensors such as AVHRR and MODIS with ideal temporal resolution, and that of field-based FLIR data with ideal spatial resolution. They would also provide a wealth of scientific information on lava flows, dome growth, pyroclastic flow and lahar emplacement, and plume dynamics at other volcanoes around the world.

ACKNOWLEDGMENTS

This research was made possible through the National Aeronautics and Space Administration (NASA) Earth System Science Research Program (grants NNG04GO69G and NNX08AJ91G) to Ramsey, as well as the support of the Advanced Spaceborne Thermal Emission and Reflection Radiometer (ASTER) Science Team. Anderson acknowledges support from grant NNG05GL55G from the NASA Mars Fundamental Research Program. The Alaska Volcano Observatory provided additional support for Wessels, and Kamchatka Volcano Eruption Response Team (KVERT)/Russian Institute of Volcanology and Seismology (IVS) provided logistical support for all the field work in Kamchatka. The quality and accuracy of this manuscript were greatly improved by the detailed comments of two anonymous reviewers, as well as those from the Associate Editor.

REFERENCES CITED

Anderson, S.W., and Fink, J.H., 1990, The development and distribution of lava textures at the Mount St. Helens dome, *in* Fink, J.H., ed., Lava Flows and Domes: Emplacement Mechanisms and Hazard Implications: International Association of Volcanology and Chemistry of the Earth's Interior (IAVCEI) Proceedings in Volcanology, v. 2, p. 25–46.

Anderson, S.W., and Fink, J.H., 1992, Crease structures; indicators of emplacement rates and surface stress regimes of lava flows: Geological Society of America Bulletin, v. 104, p. 615–625, doi:10.1130/0016-7606(1992)104<0615:CSIOER>2.3.CO;2.

Anderson, S.W., Fink, J.H., and Rose, W.I., 1995, Mount St. Helens and Santiaguito lava domes: The effect of short-term eruption rate on surface texture and degassing processes: Journal of Volcanology and Geothermal Research, v. 69, p. 105–116, doi:10.1016/0377-0273(95)00022-4.

Bailey, J.E., Dean, K., Dehn, J., and Webley, P., 2010. Integrated satellite observations of the 2006 eruptions of Augustine volcano, *in* Power, J.A., Coombs, M.L., and Freymueller, J.T., eds., The 2006 Eruption of Augustine Volcano, Alaska: U.S. Geological Survey Professional Paper 1769, p. 481–506.

Ball, M., and Pinkerton, H., 2006, Factors affecting the accuracy of thermal imaging cameras in volcanology: Journal of Geophysical Research, v. 111, p. 1–14, doi:10.1029/2005JB003829.

Belousov, A.B., 1995, The Shiveluch volcanic eruption of 12 November 1964—Explosive eruption provoked by failure of the edifice: Journal of Volcanology and Geothermal Research, v. 66, p. 357–365, doi:10.1016/0377-0273(94)00072-O.

Belousov, A., Belousova, M., and Voight, B., 1999, Multiple edifice failures, debris avalanches and associated eruptions in the Holocene history of Shiveluch volcano, Kamchatka, Russia: Bulletin of Volcanology, v. 61, p. 324–342, doi:10.1007/s004450050300.

Bulletin Global Volcanism Network (BGVN), 2005a, Shiveluch Volcano: Washington, D.C., Smithsonian Institution, v. 30, issue 02.

Bulletin Global Volcanism Network (BGVN), 2005b, Shiveluch Volcano: Washington, D.C., Smithsonian Institution, v. 30, issue 06.

Bulletin Global Volcanism Network (BGVN), 2005c, Shiveluch Volcano: Washington, D.C., Smithsonian Institution, v. 30, issue 08.

Calvari, S., Spampinato, L., Lodato, L., Harris, A.J.L., Patrick, M.R., Dehn, J., Burton, M.R., and Andronico, D., 2005, Chronology and complex volcanic processes during the 2002–2003 flank eruption at Stromboli volcano (Italy) reconstructed from direct observations and surveys with a handheld thermal camera: Journal of Geophysical Research, v. 110, p. 1–23.

Carter, A.J., and Ramsey, M.S., 2009, ASTER- and field-based observations at Bezymianny volcano: Focus on the 11 May 2007 pyroclastic flow deposit: Remote Sensing of Environment, v. 113, p. 2142–2151, doi:10.1016/j.rse.2009.05.020.

Carter, A.J., and Ramsey, M.S., 2010, Long-term volcanic activity at Shiveluch volcano: Nine years of ASTER spaceborne thermal infrared observations: Remote Sensing, v. 2, p. 2571–2583, doi:10.3390/rs2112571.

Carter, A.J., Ramsey, M.S., and Belousov, A.B., 2007, Detection of a new summit crater on Bezymianny volcano lava dome: Satellite and field-based thermal data: Bulletin of Volcanology, v. 69, p. 811–815, doi:10.1007/s00445-007-0113-x.

Carter, A.J., Girina O.A., Ramsey, M.S., and Demyanchuk, Yu., 2008, ASTER and field observations of the 24 December 2006 eruption of Bezymianny volcano, Russia: Remote Sensing of Environment, v. 112, p. 2569–2577, doi:10.1016/j.rse.2007.12.001.

Crisp, J., and Baloga, S., 1990, A method for estimating eruption rates of planetary lava flows: Icarus, v. 85, p. 512–515, doi:10.1016/0019-1035(90)90129-W.

Dehn, J., Dean, K.G., and Engle, K., 2000, Thermal monitoring of North Pacific volcanoes from space: Geology, v. 28, p. 755–758, doi:10.1130/0091-7613(2000)28<755:TMONPV>2.0.CO;2.

Dehn, J., Dean, K.G., Engle, K., and Izbekov, P., 2002, Thermal precursors in satellite images of the 1999 eruption of Shishaldin volcano: Bulletin of Volcanology, v. 64, p. 525–534, doi:10.1007/s00445-002-0227-0.

Diefenbach, A.K., Bull, K.F., Wessels, R.L., and McGimsey, R., 2012, Photogrammetric monitoring of lava dome growth during the 2009 eruption of Redoubt volcano: Journal of Volcanology and Geothermal Research, doi:10.1016/j.jvolgeores.2011.12.00.

Dirksen, O., Humphreys, M.C.S., Pletchov, P., Melnik, O., Demyanchuk, Y., Sparks, R.S.J., and Mahony, S., 2006, The 2001–2004 dome-forming eruption of Shiveluch volcano, Kamchatka: Observation, petrological investigation and numerical modeling: Journal of Volcanology and Geothermal Research, v. 155, p. 201–226, doi:10.1016/j.jvolgeores.2006.03.029.

Duda, K.A., Ramsey, M., Wessels, R., and Dehn, J., 2009, Optical satellite volcano monitoring: A multi-sensor rapid response system, *in* Ho, P.P., ed., Geoscience and Remote Sensing: Vukovar, Croatia, IN-TECH Press, p. 473–496.

Edgett, K.S., and Christensen, P.R., 1991, The particle size of Martian aeolian dunes: Journal of Geophysical Research, v. 96, p. 22,765–22,776, doi:10.1029/91JE02412.

Fedotov, S.A., and Masurenkov, Y.P., 1991, Active Volcanoes of Kamchatka, Volume 1: Moscow, Nauka, 713 p.

Feely, K.C., and Christensen, P.R., 1999, Quantitative compositional analysis using thermal emission spectroscopy: Application to igneous and metamorphic rocks: Journal of Geophysical Research, v. 104, p. 24,195–24,210, doi:10.1029/1999JE001034.

Fink, J.H., and Manley, C.R., 1987, Origin of pumiceous and glassy textures in rhyolite flows and domes, *in* Fink, J.H., ed., The Emplacement of Silicic Domes and Lava Flows: Geological Society of America Special Paper 212, p. 77–88.

Fink, J.H., Anderson, S.W., and Manley, C.R., 1992, Textural constraints on effusive silicic volcanism: Beyond the permeable foam model: Journal of Geophysical Research, v. 97, p. 9073–9083, doi:10.1029/92JB00416.

Flynn, L.P., Harris, A.J.L., and Wright, R., 2001, Improved identification of volcanic features using Landsat 7 ETM+: Remote Sensing of Environment, v. 78, p. 180–193, doi:10.1016/S0034-4257(01)00258-9.

Gillespie, A.R., and Kahle, A.B., 1977, Construction and interpretation of a digital thermal inertia image: Photogrammetric Engineering and Remote Sensing, v. 43, p. 983–1000.

Gillespie, A.R., Rokugawa, S., Matsunaga, T., Cothern, J.S., Hook, S.J., and Kahle, A.B., 1998, A temperature and emissivity separation algorithm for Advanced Spaceborne Thermal Emission and Reflection Radiometer (ASTER) images: IEEE Transactions on Geoscience and Remote Sensing, v. 36, p. 1113–1126, doi:10.1109/36.700995.

Girina, O.A., Senyukov, S.L., Demyunchuk, Y.V., Khubunaya, S.A., and Ushakov, S.A., 2004, The eruption of Sheveluch volcano, Kamchatka, on May 09, 2004: Proceedings of the 4th Biennial Workshop on Subduction Processes in the Japan-Kurile-Kamchatka-Aleutian Arcs: Petropavlovsk-Kamchatsky, Russian Academy of Sciences, p. 17.

Girina, O.A., Manevich, A.G., Malik, N.A., Melnikov, D.V., Ushakov, S.V., Demyanchuk, Y.V., and Kotenko, L.V., 2007, Active volcanoes of Kamchatka and northern Kurils in 2005: Journal of Volcanology and Seismology, v. 1, p. 237–247.

Hamilton, V.E., and Christensen, P.R., 2000, Determining the modal mineralogy of mafic and ultramafic rocks using thermal emission spectroscopy: Journal of Geophysical Research, v. 105, p. 9717–9733, doi:10.1029/1999JE001113.

Harris, A.J.L., and Stevenson, D.S., 1997, Magma budgets and steady-state activity of Vulcano and Stromboli volcanoes: Geophysical Research Letters, v. 24, p. 1043–1046, doi:10.1029/97GL00861.

Harris, A.J.L., Butterworth, A.L., Carlton, R.W., Downey, I., Miller, P., Navaro, P., and Rothery, D.A., 1997, Low-cost volcano surveillance from space: Case studies from Etna, Krafla, Cerro Negro, Fogo, Lascaar and Erebus: Bulletin of Volcanology, v. 59, p. 49–64, doi:10.1007/s004450050174.

Harris, A.J.L., Flynn, L.P., Keszthelyi, L., Mouginis-Mark, P.J., Rowland, S.K., and Resing, J.A., 1998, Calculation of lava effusion rates from Landsat TM data: Bulletin of Volcanology, v. 60, p. 52–71, doi:10.1007/s004450050216.

Harris, A.J.L., Dehn, J., Patrick, M., Calvari, S., Ripepe, M., and Lodato, L., 2005, Lava effusion rates from hand-held thermal infrared imagery: An example from the June 2003 effusive activity at Stromboli: Bulletin of Volcanology, v. 68, p. 107–117, doi:10.1007/s00445-005-0425-7.

Harris, A.J.L., Dehn, J., and Calvari, S., 2007, Lava effusion rate definition and measurement: A review: Bulletin of Volcanology, v. 70, p. 1–22, doi:10.1007/s00445-007-0120-y.

Kirianov, V.Y., Neal, C.A., Gordeev, E.I., and Miller, T.P., 2002, KVERT (Kamchatkan Volcanic Eruptions Response Team): U.S. Geological Survey Fact Sheet 064–02 (in English and Russian); also online (http://geopubs.wr.usgs.gov/fact-sheet/fs064-02/).

Lyon, R.J.P., 1965, Analysis of rocks by spectral infrared emission (8 to 25 microns): Economic Geology and the Bulletin of the Society of Economic Geologists, v. 60, p. 715–736, doi:10.2113/gsecongeo.60.4.715.

McGimsey, R.G., Neal, C.A., Dixon, J.P., and Ushakov, Sergey, 2007, 2005 Volcanic Activity in Alaska, Kamchatka, and the Kurile Islands: Summary of Events and Response of the Alaska Volcano Observatory: U.S. Geological Survey Scientific Investigations Report 2007–5269, 94 p.

National Research Council (NRC), 2007, Earth Science and Applications from Space: National Imperatives for the Next Decade and Beyond: Washington, D.C., National Academies Press, p. 113–115.

Neal, C., Girina, O., Senyukov, S., Rybin, A., Osiensky, J., Izbekov, P., and Ferguson, G., 2009, Russian eruption warning systems for aviation: Natural Hazards, v. 51, p. 245–262, doi:10.1007/s11069-009-9347-6.

Oppenheimer, C.M., and Rothery, D.A., 1991, Infrared monitoring of volcanoes by satellite: Journal of the Geological Society of London, v. 148, p. 563–569, doi:10.1144/gsjgs.148.3.0563.

Pieri, D.C., and Baloga, S.M., 1986, Eruption rate, area, and length relationships for some Hawaiian lava flows: Journal of Volcanology and Geothermal Research, v. 30, p. 29–45, doi:10.1016/0377-0273(86)90066-1.

Pieri, D.C., Glaze, L.S., and Abrams, M.J., 1990, Thermal radiance observations of an active lava flow during the June 1984 eruption of Mount Etna: Geology, v. 18, p. 1018–1022, doi:10.1130/0091-7613(1990)018<1018:TROOAA>2.3.CO;2.

Ponomareva, V.V., Pevzner, M.M., and Melekestsev, I.V., 1998, Large debris avalanches and associated eruptions in the Holocene eruptive history of Shiveluch volcano, Kamchatka, Russia: Bulletin of Volcanology, v. 59, p. 490–505, doi:10.1007/s004450050206.

Ramsey, M.S., and Christensen, P.R., 1998, Mineral abundance determination: Quantitative deconvolution of thermal emission spectra: Journal of Geophysical Research, v. 103, p. 577–596, doi:10.1029/97JB02784.

Ramsey, M.S., and Dehn, J., 2004, Spaceborne observations of the 2000 Bezymianny, Kamchatka eruption: The integration of high-resolution ASTER data into near real-time monitoring using AVHRR: Journal of Volcanology and Geothermal Research, v. 135, p. 127–146, doi:10.1016/j.jvolgeores.2003.12.014.

Ramsey, M.S., and Fink, J.H., 1999, Estimating silicic lava vesicularity with thermal remote sensing: A new technique for volcanic mapping and monitoring: Bulletin of Volcanology, v. 61, p. 32–39, doi:10.1007/s004450050260.

Ramsey, M.S., Christensen, P.R., Lancaster, N., and Howard, D.A., 1999, Identification of sand sources and transport pathways at the Kelso Dunes, California, using thermal infrared remote sensing: Geological Society of America Bulletin, v. 111, p. 646–662, doi:10.1130/0016-7606(1999)111<0646:IOSSAT>2.3.CO;2.

Ramsey, M.S., Dehn, J., Wessels, R., Byrnes, J., Duda, K., Maldonado, L., and Dwyer, J., 2004, The ASTER emergency scheduling system: A new project linking near-realtime satellite monitoring of disasters to the acquisition of high-resolution remote sensing data: Eos (Transactions, American Geophysical Union), v. 85, Fall Meeting supplement, abstract SF23A–0026.

Ramsey, M.S., Anderson, S., and Wessels, R., 2008, Active dome and pyroclastic flow deposits of Sheveluch volcano, Kamchatka: Unique thermal infrared and morphologic field observations: Reykjavík, Iceland, International Association of Volcanology and Chemistry of the Earth's Interior (IAVCEI) General Assembly Abstracts with Programs, p. 67.

Rose, S.R., and Ramsey, M.S., 2009, The 2005 eruption of Kliuchevskoi volcano: Chronology and processes derived from ASTER spaceborne and field-based data: Journal of Volcanology and Geothermal Research, v. 184, p. 367–380, doi:10.1016/j.jvolgeores.2009.05.001.

Rose, S.R., 2010, Thermal Infrared Remote Sensing of Active Basaltic Volcanoes: A Thermal and Spectral Deconvolution Approach [Ph.D. dissertation]: Pittsburgh, Pennsylvania, University of Pittsburgh, 205 p.

Rose, W.I., 1987, Volcanic activity at Santiaguito volcano, 1976–1984, *in* Fink, J.H., ed., The Emplacement of Silicic Domes and Lava Flows: Geological Society of America Special Paper 212, p. 17–27.

Ruff, S.W., 1998, Quantitative Thermal Infrared Emission Spectroscopy Applied to Granitoid Petrology [Ph.D. thesis]: Tempe, Arizona State University, 234 p.

Salisbury, J.W., and Walter, L.S., 1989, Thermal infrared (2.5–13.5 μm) spectroscopic remote sensing of igneous rock types on particulate planetary surfaces: Journal of Geophysical Research, v. 94, p. 9192–9202, doi:10.1029/JB094iB07p09192.

Scheidt, S., Ramsey, M.S., and Lancaster, N., 2010, Determining soil moisture and sediment availability at White Sands Dune Field, NM, from apparent thermal inertia (ATI) data: Journal of Geophysical Research, v. 115, F02019, doi:10.1029/2009JF001378.

Scheidt, S., Ramsey, M., and Lancaster, N., 2011, Eolian dynamics and sediment mixing in the Gran Desierto, Sonora, Mexico: Fusion of infrared orbital and emission spectroscopy data: Geological Society of America Bulletin, v. 123, p. 1628–1644, doi:10.1130/B30338.1.

Schneider, D., Vallance, J., Wessels, R., Logan, M., and Ramsey, M., 2009, Use of thermal infrared imaging for monitoring renewed dome growth at Mount St. Helens, 2004, *in* Sherrod, D.R., Scott, W.E., and Stauffer, P.H., eds., A Volcano Rekindled: The Renewed Eruption of Mount St. Helens, 2004–2006: U.S. Geological Survey Professional Paper 1750, p. 347–359.

Senyukov, S.L., Droznina, S.Y., Nuzhdina, I.N., Garbuzova, V.T., and Kozhevnikova, T.U., 2009, Studies in the activity of Klyuchevskoi volcano by remote sensing techniques between January 1, 2001 and July 31, 2005: Journal of Volcanology and Seismology, v. 3, p. 191–199, doi:10.1134/S0742046309030051.

Swanson, D.A., Dzurisin, D., Holcomb, R.T., Iwatsubo, E.Y., Chadwick, W.W., Casadevall, T.J., Ewert, J.W., and Heliker, C.C., 1987, Growth of the lava dome at Mount St. Helens, Washington, (USA), 1981–1983, *in* Fink, J.H., ed., The Emplacement of Silicic Domes and Lava Flows: Geological Society of America Special Paper 212, p. 17–27.

Thome, K., Palluconi, F., Takashima, T., and Masuda, K., 1998, Atmospheric correction of ASTER: IEEE Transactions on Geoscience and Remote Sensing, v. 36, p. 1199–1211, doi:10.1109/36.701026.

Urai, M., Fukui, K., Yamaguchi, Y., and Pieri, D.C., 1999, Volcano observation potential and global volcano monitoring plan with ASTER: Bulletin of the Volcanological Society of Japan, v. 44, p. 131–141.

Vaughan, R.G., and Hook, S.J., 2006, Using satellite data to characterize the temporal thermal behavior of an active volcano: Mount St. Helens, WA: Geophysical Research Letters, v. 33, doi:10.1029/2006GL027957.

Vaughan, R.G., Hook, S.J., Ramsey, M.S., Realmuto, V.J., and Schneider, D.J., 2005, Monitoring eruptive activity at Mount St. Helens with TIR image data: Geophysical Research Letters, v. 32, doi:10.1029/2005GL024112.

Watson, I.M., Oppenheimer, C., Voight, B., Francis, P.W., Clarke, A., Stix, J., Miller, A., Pyle, D.M., Burton, M.R., Young, S.R., Norton, G., Loughlin, S., Darroux, B., and Staff, M.V.O., 2000, The relationship between degassing and ground deformation at Soufriere Hills volcano, Montserrat: Journal of Volcanology and Geothermal Research, v. 98, p. 117–126, doi:10.1016/S0377-0273(99)00187-0.

Watson, I.M., Realmuto, V.J., Rose, W.I., Prata, A.J., Bluth, G.S., Gu, Y., Bader, C.E., and Yu, T., 2004, Thermal infrared remote sensing of volcanic emissions using the moderate resolution imaging spectroradiometer: Journal of Volcanology and Geothermal Research, v. 135, p. 75–89, doi:10.1016/j.jvolgeores.2003.12.017.

Wessels, R.L., Schneider, D.J., Coombs, M.L., Dehn, J., and Ramsey, M.S., 2010, High-resolution satellite and airborne thermal infrared imaging of the 2006 eruption of Augustine volcano, Alaska, *in* Power, J.A., Coombs, M.L., and Freymueller, J.T., eds., The 2006 Eruption of Augustine Volcano, Alaska: U.S. Geological Survey Professional Paper 1769, p. 527–553.

Wessels, R.L., Bull, K.F., McGimsey, R.G., Diefenbach, A.K., Coombs, M.L., and Schneider, D.J., 2009, High resolution satellite and airborne thermal infrared (TIR) imaging of the 2009 eruption of Redoubt Volcano, Alaska: Eos [Transactions, American Geophysical Union], v. 90, Fall Meeting, Abstract V51F-07.

Wright, R., and Flynn, L., 2003, On the retrieval of lava-flow surface temperatures from infrared satellite data: Geology, v. 31, p. 893–896, doi:10.1130/G19645.1.

Wright, R., Blake, S., Harris, A.J.L., and Rothery, D.A., 2001, A simple explanation for the space-based calculation of lava eruption rates: Earth and Planetary Science Letters, v. 192, p. 223–233, doi:10.1016/S0012-821X(01)00443-5.

Wright, R., Flynn, L., Garbeil, H., Harris, A., and Pilger, E., 2002, Automated volcanic eruption detection using MODIS: Remote Sensing of Environment, v. 82, p. 135–155, doi:10.1016/S0034-4257(02)00030-5.

Wright, R., Carn, S.A., and Flynn, L.P., 2005, A satellite chronology of the May–June 2003 eruption of Anatahan volcano: Journal of Volcanology and Geothermal Research, v. 146, p. 102–116, doi:10.1016/j.jvolgeores.2004.10.021.

Wyatt, M.B., and McSween, H.Y., 2002, Spectral evidence for weathered basalt as an alternative to andesite in the northern lowlands of Mars: Nature, v. 417, p. 263–266, doi:10.1038/417263a.

Yamaguchi, Y., Kahle, A.B., Tsu, H., Kawakami, T., and Pniel, M., 1998, Overview of Advanced Spaceborne Thermal Emission and Reflection Radiometer (ASTER): IEEE Transactions on Geoscience and Remote Sensing, v. 36, p. 1062–1071, doi:10.1109/36.700991.

Zharinov, N., and Demyanchuk, Y., 2008, The growth of extrusive dome on Shiveluch Volcano, Kamchatka in 1980–2007: Geodetic observations and video surveys: Journal of Volcanology and Seismology, v. 2, p. 217–227, doi:10.1134/S0742046308040015.

Science Editor: Nancy Riggs
Associate Editor: Chris Newhall

Manuscript Received 30 July 2011
Revised Manuscript Received 11 October 2011
Manuscript Accepted 20 October 2011

Printed in the USA